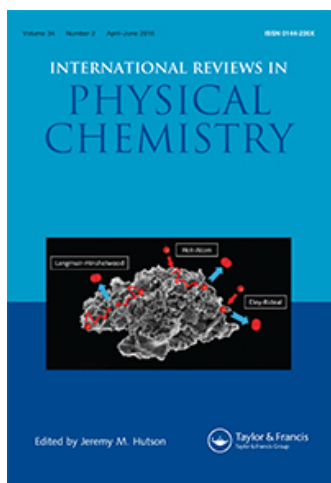


This article was downloaded by: [University of California, Berkeley]

On: 26 August 2015, At: 10:09

Publisher: Taylor & Francis

Informa Ltd Registered in England and Wales Registered Number: 1072954 Registered office: 5 Howick Place, London, SW1P 1WG



International Reviews in Physical Chemistry

Publication details, including instructions for authors and subscription information:

<http://www.tandfonline.com/loi/trpc20>

Ultrafast electronic dynamics in helium nanodroplets

Michael P. Ziemkiewicz^{ab}, Daniel M. Neumark^{ab} & Oliver Gessner^a

^a Ultrafast X-ray Science Laboratory, Chemical Sciences Division, Lawrence Berkeley National Laboratory, Berkeley, CA 94720, USA

^b Department of Chemistry, University of California, Berkeley, CA 94720, USA

Published online: 06 Jul 2015.



CrossMark

[Click for updates](#)

To cite this article: Michael P. Ziemkiewicz, Daniel M. Neumark & Oliver Gessner (2015) Ultrafast electronic dynamics in helium nanodroplets, *International Reviews in Physical Chemistry*, 34:2, 239-267, DOI: [10.1080/0144235X.2015.1051353](https://doi.org/10.1080/0144235X.2015.1051353)

To link to this article: <http://dx.doi.org/10.1080/0144235X.2015.1051353>

PLEASE SCROLL DOWN FOR ARTICLE

Taylor & Francis makes every effort to ensure the accuracy of all the information (the "Content") contained in the publications on our platform. However, Taylor & Francis, our agents, and our licensors make no representations or warranties whatsoever as to the accuracy, completeness, or suitability for any purpose of the Content. Any opinions and views expressed in this publication are the opinions and views of the authors, and are not the views of or endorsed by Taylor & Francis. The accuracy of the Content should not be relied upon and should be independently verified with primary sources of information. Taylor and Francis shall not be liable for any losses, actions, claims, proceedings, demands, costs, expenses, damages, and other liabilities whatsoever or howsoever caused arising directly or indirectly in connection with, in relation to or arising out of the use of the Content.

This article may be used for research, teaching, and private study purposes. Any substantial or systematic reproduction, redistribution, reselling, loan, sub-licensing, systematic supply, or distribution in any form to anyone is expressly forbidden. Terms &

Conditions of access and use can be found at <http://www.tandfonline.com/page/terms-and-conditions>

Ultrafast electronic dynamics in helium nanodroplets

Michael P. Ziemkiewicz^{a,b}, Daniel M. Neumark^{a,b} and Oliver Gessner^{a*} 

^aUltrafast X-ray Science Laboratory, Chemical Sciences Division, Lawrence Berkeley National Laboratory, Berkeley, CA 94720, USA; ^bDepartment of Chemistry, University of California, Berkeley, CA 94720, USA

(Received 1 March 2015; final version received 24 March 2015)

Helium nanodroplets have emerged as a test bed for the study of isolated quantum liquids and as an ideal matrix for trapping atoms and molecules in a weakly interacting, cryogenic environment. Their high transparency at visible and infrared wavelengths facilitates the study of dissolved species with traditional spectroscopy techniques. At photon energies above ~21 eV, however, the droplets themselves begin to absorb to form complex excited states that have proven a challenge for both experiment and theory. A variety of frequency- and time-domain methods have been used to characterise electronically excited droplet states and their relaxation channels. This review focuses on a recent series of time-domain experimental studies that have revealed several phenomena such as interband relaxation dynamics within the droplet environment, and provided deeper insight into previously detected relaxation channels, including the ejection of Rydberg atoms (He^*) and molecules (He_n^*), the dynamics of highly excited droplet states, and photoassociation to produce strongly-bound excimer species (such as He_2^*). A brief outline of corresponding *ab initio* efforts for the theoretical description of electronically excited He droplet states and their relaxation dynamics will also be given.

Keywords: helium nanodroplets; superfluid; ultrafast dynamics; photoassociation; electronic relaxation; solvated Rydberg atoms; exciplexes

Contents	PAGE
1. Introduction	240
2. Experimental techniques – energy-domain	241
3. Experimental techniques – time-domain	243
4. Electronic spectroscopy of pure helium droplets	244
5. Photoionisation and photoelectron spectroscopy of helium nanodroplets	246
6. Near-surface dynamics and Rydberg atom ejection	249
7. Dynamics within the droplet bulk	255
8. Interband relaxation	258

*Corresponding author. Email: ogessner@lbl.gov

9. Ejection of molecular species from droplets	260
10. Summary and prospects	263
Disclosure statement	264
References	264

1. Introduction

Liquid helium is a fascinating state of matter. The bosonic nature of ^4He atoms, their very weak atom–atom attractive dispersive force, and their low masses are enabling factors for unusual behaviour when cooled below the lambda point (~ 2.2 K) into the superfluid state [1–4]. Even above this temperature, liquid helium is unique compared to other noble gas clusters in that the average atom–atom spacing (~ 3.6 Å) is defined by the zero point energy of its constituent atoms confined by their neighbours rather than by the van der Waals radius of atomic He (~ 1.1 Å) [5–11]. The characteristic internuclear distance in liquid helium is also large compared to the atoms' electron scattering cross section [2]. This property, combined with the repulsive interaction between free low energy electrons and neutral helium atoms, results in a 'conduction band' in the liquid with an onset ~ 1 eV above the vacuum level and characterised by electronic wavefunctions confined to the interstitial spaces between atoms [2,12–17]. Liquid He also supports localised electronic excitations involving single atoms where the majority of the wavefunction is still mostly confined to the nearest neighbour distance [18]. The exact behaviour of excited electrons in this material is a matter of intense study using a variety of different techniques [2,19,20]. Of particular interest is the structure and timescale for electronic and atomic rearrangements resulting from these electronic excitations [21]. Other aspects of the study of helium nanodroplets have been the subject of excellent recent review articles covering topics such as spectroscopy in the nano-confined, superfluid environment [22], dynamics of electronically excited doped droplets [23], and cryo-chemistry in the helium nanomatrix [24]. This review focuses on electronic excitations in liquid He nanodroplets.

By cooling high pressure (~ 20 – 80 bar) helium to very low temperatures (~ 5 – 20 K) prior to introducing it into a vacuum chamber by a free jet expansion, He atoms spontaneously condense into droplets with a reasonably well-defined average diameter that can be precisely controlled by varying the nozzle temperature and backing pressure [25–27]. Droplet sizes may be varied over nano to micron scales (~ 10 nm– 1 μm). Superfluid helium nanodroplets have gained particular attention for their ability to trap and cool dopant atoms and molecules for spectroscopic studies in a cryogenic, weakly interacting environment [22,28–36]. Moreover, the trapping of multiple atoms and/or molecules can be employed to study reaction dynamics and cluster formation under cryogenic conditions [24,31,37–43]. Droplets are also capable of supporting unique electronically excited states of surface-bound dopants leading to unusual Rydberg levels [44–46]. Additionally, as size-tunable nanoscale objects, droplets provide a testing ground for the distinction of surface and bulk effects because their size can be chosen to be in a regime where the majority of atoms is located either within a monolayer below the surface or in the droplet bulk [8,47]. Most recently, rotating helium droplets have also been employed to study the emergence of quantum vortex lattices and new regimes of high rotational excitations in isolated quantum liquids [4].

Rather high energies are needed to electronically excite helium nanodroplets, mirroring the high energy (19.8 eV) of the first excited state of gas phase He [48,49]. Early studies employed electron impact excitation and ionisation techniques in order to access these energies [50–53]. To excite pure He droplets optically, one requires intense light sources in the extreme ultraviolet (EUV) range of the electromagnetic spectrum. This light is available at synchrotron radiation sources where it can be finely tuned to map out the structure of the electronically excited states and characterise the fluorescence, ions, and photoelectrons that are produced during their relaxation. Section 2 of this review presents the experimental techniques used to perform these studies while Sections 4 and 5 provide a brief overview of the corresponding results, with an emphasis on those which hint at the nature of relaxation processes occurring in the electronically excited system.

Energy-domain studies are complemented by time-domain studies in which a femtosecond EUV light pulse is created by high-harmonic generation (HHG) [54]. A variety of pump–probe experiments [23,55] are described that monitor the time-evolution of relaxation pathways within the droplet environment following EUV excitation [56–60]. These studies are capable of confirming pictures that are suggested by the energy-domain results. They also reveal transient intermediate states that would not be detectable in energy-domain experiments. The focus of this publication is to provide an overview of what has been learned from direct time-domain measurements on the electronic structure and excited state dynamics of pure and doped helium nanodroplets. Section 3 introduces experimental techniques used to perform these studies. Section 6 focuses on a relaxation channel involving the ejection of Rydberg-excited atoms. Section 7 summarises results concerning the nature of the initial state of a resonantly excited helium nanodroplet and its decay. Section 8 focuses on strong indications of an efficient interband electronic relaxation channel. Section 9 concerns the ubiquitous process where droplet photoexcitation induces chemical bonding to produce electronically excited molecular complexes (‘exciplexes’). Section 10 summarises this review and provides a brief perspective on the future of studying the fate of excited electrons in helium nanodroplets.

2. Experimental techniques – energy-domain

The physical properties of pure and doped He nanodroplets have been studied with a variety of methods based on electron impact [50], droplet beam depletion [26], molecular beam scattering [8], strong-field ionisation [61], droplet matter-wave diffraction [62], and X-ray coherent scattering [4]. Here, we concentrate on photon-based experimental techniques used to explore the electronic structure of helium nanodroplets and the dynamics induced by electronic excitation. A pivotal point for the study of electronic excitations and dynamics in helium droplets was the work of the Möller group, in which high-resolution, synchrotron-based single photon excitation beyond 20 eV was combined with EUV fluorescence yield detection, effectively enabling the first recording of the droplet EUV absorption spectrum [49]. The same group subsequently extended the power of the method by energy-dispersed fluorescence detection in the visible and infrared (IR) regimes using a Czerny–Turner spectrometer. This capability facilitated the detailed characterisation of atomic and molecular complexes resulting from droplet relaxation as discussed in Section 4.

Toennies and collaborators performed the first photoionisation study on pure helium nanodroplets using photon energies up to 30 eV [63]. The Neumark group extended this work by synchrotron-based photoelectron imaging experiments [64,65]. Figure 1 shows the apparatus used in these studies. Helium droplets are generated by expanding gaseous or liquid helium through a cryogenically cooled, 5 μm wide, aperture into a high vacuum chamber. Stagnation pressures and nozzle temperatures may vary across ranges of ~ 20 –80 bar and ~ 5 –40 K, respectively, leading to average droplet sizes $\langle N \rangle$ between hundreds and tens of millions of atoms [22]. The droplets pass through a small skimmer into a differentially pumped chamber in which they traverse a gas cell where they may pick up dopant atoms and molecules. Passing through a second small skimmer, the droplet beam enters the interaction chamber where it intersects the light beam in the interaction region of a photoelectron velocity map imaging (VMI) setup [66]. The recorded images simultaneously provide both kinetic energy (KE) and angular distributions of the emitted photoelectrons.

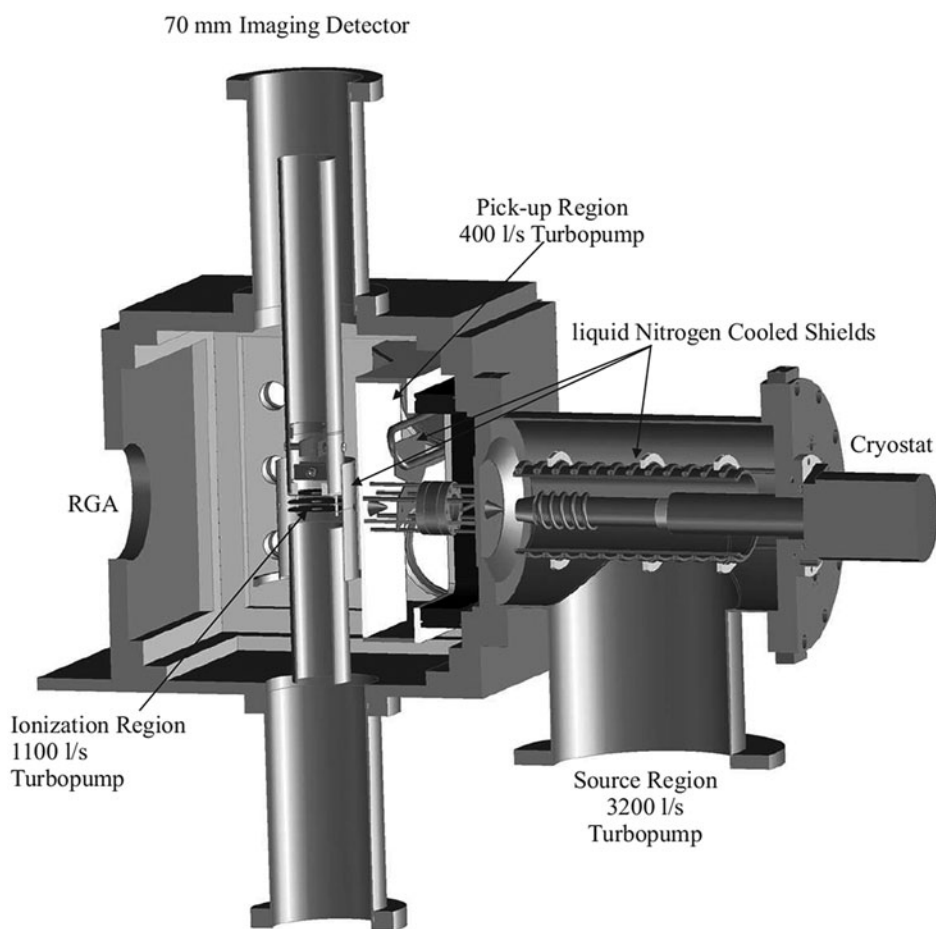


Figure 1. Experimental apparatus used to deliver helium droplets to an interaction volume where they intersect a beam of EUV radiation. Photoelectrons are detected using VMI. Adapted with permission from [65]. Copyright 2007, American Chemical Society.

More recently, Drabbls and coworkers [33,67] as well as Stienkemeier and coworkers [68–71] have implemented various electron and ion imaging schemes as well as electron-ion coincidence techniques that have been successfully employed to monitor a variety of phenomena, including charge transfer and Penning ionisation in doped helium droplets [69] and new collective autoionisation phenomena in intense light fields [70,71].

3. Experimental techniques – time-domain

The new insight into ultrafast Helium droplet dynamics that can be gained by experiments employing femtosecond EUV light sources is one of the main motivators of this review. In particular HHG of ultrashort EUV pulses has become a powerful tool for ultrafast time-domain studies based on single-photon, high-energy excitation and/or ionisation [56,72]. Very recently, EUV- and X-ray free electron laser (FEL) based techniques have also become available [4,70].

The time-domain experiments discussed in more detail in Sections 6–9 were performed using the setup illustrated in Figure 2. A high-power Ti:Sapphire based femtosecond laser system operating at 3 kHz is used to produce femtosecond EUV pulses by HHG in a gas cell filled with Xe or Kr atoms at stagnation pressures of a few Torr. Most of the IR light that co-propagates with the EUV light is removed from the beam path by two parallel silicon blocks that are aligned at Brewster's angle for the IR beam. The IR beam mostly passes through the Si substrates while approximately half of the EUV light is reflected from the Si surfaces. The remaining IR contribution is blocked by a thin (~100 nm) Al or Sn foil that also acts as a bandpass filter for the EUV pump beam. A small fraction of the IR light emerging from the laser is split off to form the probe beam, routed through a programmable delay stage, and re-combined with the

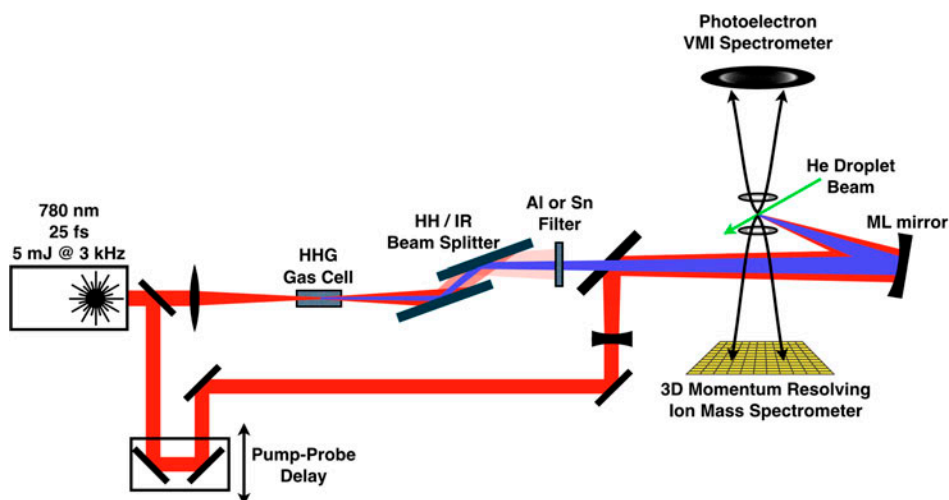


Figure 2. Schematic of experimental setup for femtosecond time-resolved photoionisation studies of helium nanodroplets. HHG is used to produce ultrashort EUV pump pulses that electronically excite droplets, which are then ionised using a second, time-delayed optical femtosecond probe pulse. Photoelectrons and ions are detected using VMI and mass-resolved ion momentum imaging, respectively [56,58].

EUV pump beam using an annular mirror. For experiments with 3.2 eV probe photons, a BBO-crystal-based second harmonic generation scheme is implemented in the probe beam path before the beam combiner [60]. The co-propagating pump and probe-beams are both reflected off the same spherically curved multilayer (ML) mirror near normal incidence. The ML mirror focuses the beams into the interaction volume of a double spectrometer setup. One side consists of the photoelectron VMI spectrometer described in Section 2 [56,57]. Alternatively, a Wiley–McLaren time-of-flight ion spectrometer [73] mounted opposite to the VMI setup and equipped with a fast time- and position-sensitive delay-line anode [74] is used to measure mass-resolved ion momenta on an event-by-event basis [58,59]. These may be translated, for example, into mass-selected ion KE distributions as described in Sections 6 and 9.

With the advent of EUV and X-ray FELs, femtosecond pulses are now available with widely tunable photon energies ranging from the lowest droplet absorption band to the hard X-ray regime [75,76]. Experiments performed at FERMI and the LCLS have so far mostly employed the high peak intensities of FELs either for the observation of novel collective autoionisation schemes [70,71] or coherent diffractive imaging of phenomena associated with quantum rotation [4]. Explicitly time-dependent experiments with helium droplets using pump–probe schemes have also been performed at FELs by several groups including ours. To the best of our knowledge, none of this work has yet been published but private communications indicate that this new generation of experiments will reveal yet another facet of coupled electronic and nuclear dynamics in excited and/or ionised helium nanodroplets.

4. Electronic spectroscopy of pure helium droplets

Using tunable synchrotron radiation, Möller and coworkers reported the first electronic spectra of pure helium nanodroplets. In these fluorescence action spectroscopy measurements, as shown in Figure 3, droplets of different sizes were exposed to tunable EUV light, and fluorescence from electronically excited droplets and ejected fragments was detected [47,49,77]. Compared to the spectrum of dense helium gas (bottom panel), droplet transitions are blue-shifted by several hundred meV, as illustrated by the sharp atomic peaks in the top and middle panels that are due to contamination by gas phase helium atoms and/or surface excitations of the droplets. The strong transition associated with $1s2p \leftarrow 1s^2$ excitations (feature B), which was previously observed in reflective absorption measurements at the surface of bulk liquid helium [20], is less blue-shifted than the one associated with $1s3p/4p \leftarrow 1s^2$ excitations (features D and E), likely due to increased quantum confinement of the more extended $1s3p/4p$ wave functions by neighbouring He atoms. Also, the spectra of the largest helium droplets (top panel) feature a long tail to higher excitation energies.

In the initial experiments, fluorescence between 15 and 25 eV was detected, much of which presumably resulted from $\text{He}^* 2p \rightarrow 1s$ emission at 21.2 eV [49]. In subsequent work, fluorescence was collected in the visible/infrared (vis/IR), enabling the observation of radiative transitions between electronically excited helium levels [78]. These studies were enhanced by adding dispersed fluorescence techniques, which provided valuable insight into the nature of the states contributing to the fluorescence from excited droplets. In pure droplets, excitation at 23.09 eV (on the low end of the $1s3p$ band) results in fluorescence dominated by several lines originating in atomic $n = 3$ levels. In addition, a higher excitation energy of 24.13 eV leads to more fluorescence at lines associated with the He_2^* excimer dimer [78]. Calculations indicate that the ground

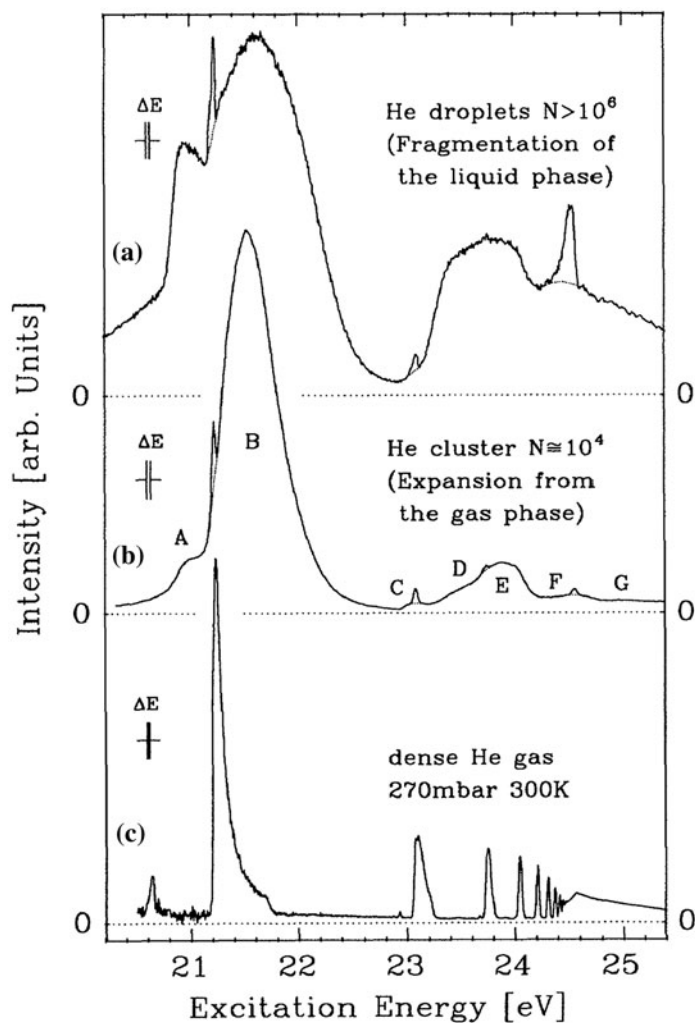


Figure 3. EUV-induced fluorescence spectra of helium droplets with mean atom numbers $N > 10^6$ (a), $N \sim 10^4$ (b), and dense gas (c). Reprinted figure with permission from [49] by the American Physical Society.

state of this species is bound by about 2 eV and essentially consists of a covalently bound He_2^+ core with a 2s Rydberg electron [79–81]. Therefore, the observation of these fluorescence lines indicates that after the droplet absorbs synchrotron radiation, a chemical relaxation channel exists that can be followed by ejection of the newly-formed He_2^* excimer. This picture was confirmed by observing IR/vis fluorescence at energies greater than 1.4 eV after direct excitation into the droplet 1s2p band at 21.6 eV [77]. Since this fluorescence photon energy is in excess of the atomic $2p \rightarrow 2s$ energy difference of 1.14 eV, it was attributed to luminescent relaxation between electronically excited molecular states (He_n^*).

The nature of these excited droplet states has recently been addressed in electronic structure calculations. The Head-Gordon group was able to reproduce the electronic

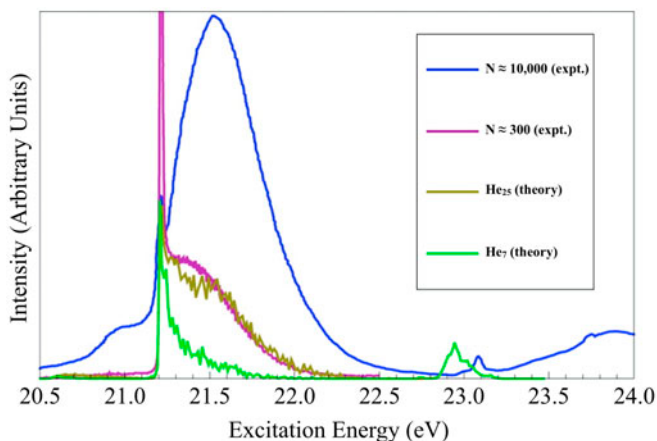


Figure 4. *Ab initio* calculations (green and brown) that simulate electronic transition energies and intensities for clusters containing a small number of atoms. For $N_{\text{atoms}} = 25$, the theory agrees well with experimental fluorescence measurements on 300 atom clusters in the $1s2p \leftarrow 1s^2$ band (pink). Adapted with permission from [18]. Copyright 2010, American Chemical Society.

absorption spectrum of small droplets in the $1s2p$ band by performing *ab initio* calculations on randomised condensates containing up to 25 atoms, as shown in Figure 4 [18]. The overall structure of the calculated band represents a series of closely spaced electronic excitations, each originating from a slightly different geometry of the model 25-atom cluster and taking into account all possible excitations associated with all atoms. Both the excitation energy and the shape of the orbital for the excited electron depend strongly on cluster geometry. Additional insight was obtained by Kornilov *et al.*, who were able to reproduce the spectrum of both the upper and the lower bands in Figure 3 using a simple heterogeneous broadening model in which quantum confinement of the excited electronic states decreases for atoms nearer to the droplet surface due to the decreasing helium density in the surface region [57]. This trend means that the $1s3p \leftarrow 1s^2$ atomic transition is minimally blue shifted at the droplet surface and much more blue-shifted for excitations deep in the droplet interior. This model also explains the observation of ejected Rydberg atoms in the synchrotron studies since such a surface energy gradient would directly lead to a radial force pushing He^* products out of the droplet and into the surrounding vacuum as will be discussed in more detail in Section 6.

5. Photoionisation and photoelectron spectroscopy of helium nanodroplets

Fröchtenicht *et al.* carried out photoionisation experiments on He droplets in which photoions and near-threshold photoelectrons were observed following synchrotron excitation in the two main droplet bands shown in Figure 3 [63]. The detected trends differed substantially from those seen in the fluorescence measurements. For example absorption in the $1s2p$ band, which dominates the EUV-induced fluorescence spectrum, does not generate a measurable yield of photoelectrons, indicating that this band lies below the droplet IP. Instead, the threshold for photoelectron production (~ 23 eV) coincides with the onset of absorption into the $1s3p$ band, the weaker of the two main

peaks seen in the experiments of the Möller group [63]. Therefore, the droplet IP lies 1.6 eV below the gas phase atomic He IP, a result that was ascribed to the chemical energy released in the formation of He_2^+ products [79–81]. Figure 5 shows results later obtained by Peterka *et al.* in the study of photoelectron energy- and angular distributions by VMI [64,82]. As seen in Figure 5(a), these photoelectron experiments confirmed the existence of a ~ 23 eV droplet IP. Furthermore, ionisation between the droplet IP at 23 eV and the atomic helium IP at 24.6 eV must be dominated by an indirect process since the droplet photoelectron energy distribution is largely independent of the photon energy in this region.

In fact, as shown in Figure 5(b), the droplet photoelectrons resulting from $1s3p/4p$ excitation are always characterised by an extremely low KE, with most having less than 1 meV [64]. Therefore, they are referred to as ‘zero electron kinetic energy’ (ZEKE) electrons. They may be the result of an alternative relaxation pathway proceeding in parallel to the one leading to the Rydberg atoms that dominate the vis/IR fluorescence results. It has been suggested that this ZEKE signal could be a result of the formation of electron bubbles in the droplets caused by atomic rearrangement in the presence of a dissolved electron, a process that is expected to occur in several ps at typical bulk liquid helium densities [12,64,83–86]. However, a similar cold electron signal has been found to be the result of field ionisation of high Rydberg atoms in a DC electric potential used to pull photoelectrons into a VMI detection system [87]. Such a process must involve very highly-excited Rydberg levels (such as those which can be produced in electron-cation recombination) since no such ZEKE peak is seen for gas phase atoms excited to lower ($n = 3$ and $n = 4$) Rydberg states [72].

Figure 6 shows the electron kinetic energy (eKE) distributions obtained when Peterka *et al.* ionised pure droplets with synchrotron radiation *above* the atomic IP (at $h\nu = 25$ eV) [65]. In contrast to the studies performed below the atomic IP, the results in Figure 6 appear to be a more direct ionisation with electron kinetic energies close to those from gas phase helium atoms (as shown in the high nozzle temperature curves in Figure 6). Interestingly, in this case the average eKE from droplets is actually about 200 meV higher than that obtained from bare atom photoionisation. Peterka *et al.* used a Monte Carlo simulation to show that this extra energy could be due to He ionisation at the fraction of sites in which two helium atoms happen to be unusually close together in the droplet, resulting in the formation of an elongated He_2^+ cation within the droplet. Consistent with Möller *et al.*'s dispersed fluorescence measurements that

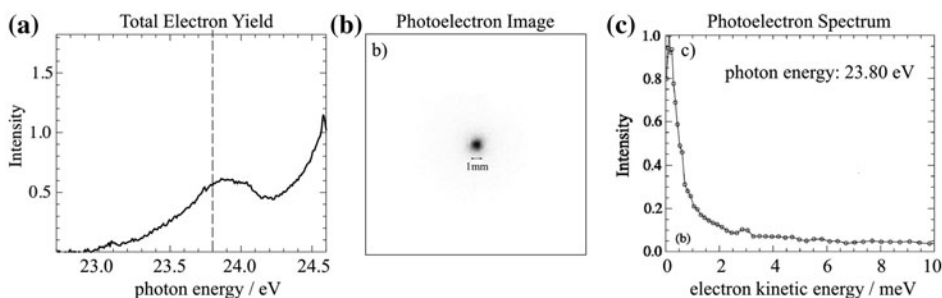


Figure 5. (a) Helium droplet photoionisation action spectrum. (b) Photoelectron image. (c) ZEKE photoelectron KE distribution for single photon excitation below the atomic IP. Reprinted figure with permission from [64] by the American Physical Society.

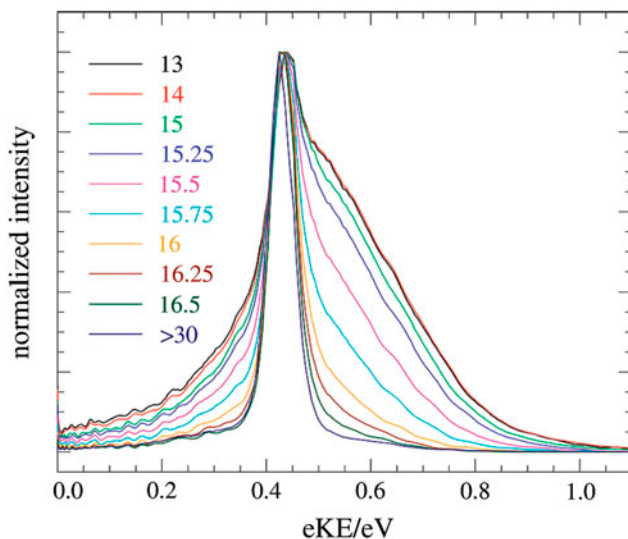


Figure 6. Photoelectron KE distributions for a range of nozzle temperatures (in Kelvin) for droplet ionisation above the atomic IP ($h\nu = 25$ eV). Reprinted with permission from [65]. Copyright 2007, American Chemical Society.

detected the formation of He_2^* , these results suggest that interaction with EUV light may also induce ionic configurations with a reduced internuclear distance compared to the average, large spacing between atoms in the droplet ground state (~ 3.6 Å) [65].

While excitation of pure droplets at the energy of the main band at 21.6 eV does not lead to ionisation, novel ionisation dynamics are observed when doped droplets are excited at this energy as it exceeds the ionisation potential (IP) of any dopant. Photoionisation mass spectrometry and photoelectron spectroscopy experiments have been carried out in doped droplets excited by synchrotron radiation at 21.6 eV [88,89]. For example, Figure 7 shows photoelectron KE distributions for droplets doped with a single Xe or Kr atom [90]. Here, signals originate from a Penning ionisation process where the initial electronic excitation in the $1s2p$ band finds its way to the dopant atom and ionises it [63,69,88,91]. The structured peak at $e\text{KE} = 6\text{--}10$ eV can be directly assigned to Penning ionisation to produce various final states of the Xe^+/Kr^+ cation left behind by the Penning electron. A similar process was observed by Stienkemeier and coworkers [69] for dopants localised either on the surface or in the bulk of small helium droplets containing between 10^2 and 10^4 atoms [69]. In that case, the Penning process was found to be considerably more efficient for the surface dopants, indicating a possible spontaneous transfer of electronic excitation radially outward from the droplet centre. In Figure 7, the broad low energy feature between 0 and ~ 7 eV is not as well understood but could be the result of an inelastic scattering process whereby the product photoelectron deposits energy into the liquid environment on its way out of the droplet. For the largest droplets studied, a gap appears between 0 and approximately 1 eV, which is likely a direct consequence of the ~ 1 eV conduction band edge characteristic of liquid He [14]. Since electrons in this energy range are not free to travel through the liquid helium matrix, they would instead be trapped in place and may decay via other channels.

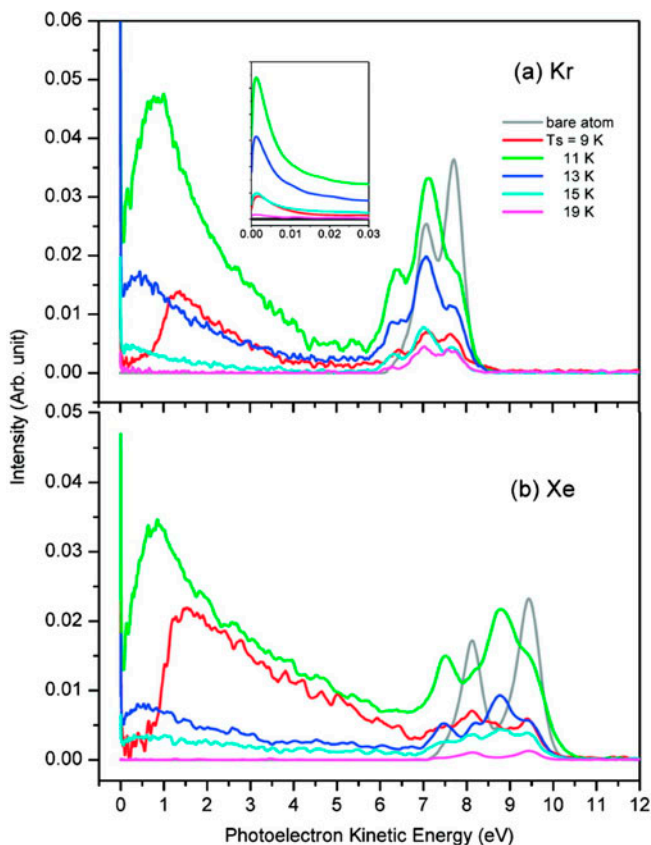


Figure 7. Energy distributions for photoelectrons generated by Penning ionisation of dopants after droplet excitation at $h\nu = 21.6$ eV for a variety of average droplet sizes as controlled by the variable nozzle temperature T_s . Reprinted with permission from [90]. Copyright 2008, American Chemical Society.

6. Near-surface dynamics and Rydberg atom ejection

The discovery of Rydberg fragment ejection by the Möller group stimulated a series of studies into both the underlying physics of this droplet cooling mechanism and the character of the electronically excited droplet states. Further fluorescence experiments by Möller and coworkers indicated the existence of localised excitations involving single helium atoms and dimers inside the droplets [21,92], the transport of excited molecules by helium bubble formation and migration [21], and a direct correlation between excitation energies and particle densities [47,92]. While a general trend emerged that associates higher excitation energies with higher particle densities, a more complex picture became apparent with respect to the existence of bulk excitations beyond 23 eV [47] and the ejection mechanism of excited species with both bubble transport from inside the bulk of large droplets on nanosecond timescales [21] as well as much faster ejection of excited surface species [78] deemed possible pathways.

Femtosecond time-resolved experiments as described in Section 3 provide the opportunity to probe the emergence of Rydberg atoms and molecules directly in the time-domain as illustrated in Figure 8. Electronic excitation of the droplet in the range

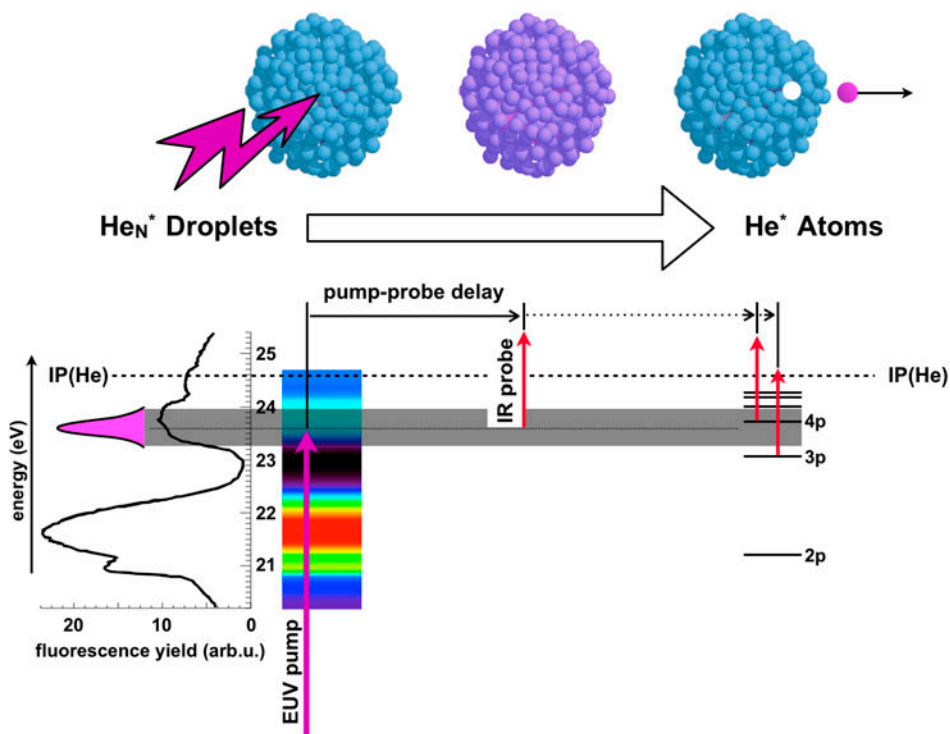


Figure 8. Energetics of EUV-pump/IR-probe studies of Rydberg-atom ejection from pure He nanodroplets. An EUV pump pulse excites droplets above their IP, but below the atomic IP. The excitation may lead to the ejection of Rydberg atoms. Both in-droplet and ejected atom states are monitored by photoionisation using a 1.6 eV probe pulse. Reprinted with permission from [59]. Copyright 2012, AIP Publishing LLC.

of the $1s3p/4p$ band is induced by a femtosecond high-harmonic (HH) pump pulse. The initially excited droplet states and, in particular, the emergence of ejected Rydberg fragments is monitored by ionising transient species with a femtosecond IR (1.6 eV) probe pulse. Pump-probe time delay dependent photoelectron and ion imaging provides detailed information on the character of the transient states as well as the timescales and kinetic energies associated with different relaxation channels.

Figure 9 shows transient photoelectron velocity map images of pure helium nanodroplets ($\langle N \rangle = 2 \times 10^6$) as a function of pump-probe delay Δt using pump and probe photon energies of 23.7 and 1.6 eV, respectively [57]. Signals associated exclusively with the pump pulse, as seen at $\Delta t = -250$ fs, have been subtracted for zero and positive delays. The isotropic, energetically broad photoelectron signal from the initially excited droplet states dominates at time zero. It is replaced by the sharp, highly anisotropic signal from emerging Rydberg atoms and molecules within a few hundred femtoseconds. These signals remain essentially unchanged on picosecond timescales, reflecting the long (\sim ns) fluorescence lifetimes of the ejected Rydberg fragments [72]. Figure 10(a) provides a more detailed picture of the time dependent energetic trends. It shows pump-probe time delay dependent photoelectron KE distributions derived from the transient VMI data. Note that the KE axis is nonlinear to better visualise signals at high and low KEs simultaneously. The broad photoelectron KE distribution of the

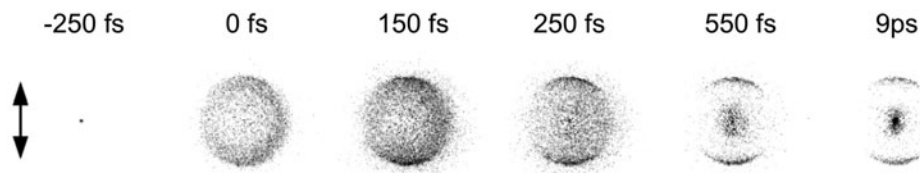


Figure 9. Raw photoelectron velocity map images of pure helium nanodroplets ($\langle N \rangle = 2 \times 10^6$) as a function of pump–probe delay, using pump- and probe-photon energies of 23.7 and 1.6 eV, respectively. The double arrow indicates the polarisation of both beams; the pump–probe delays are noted above the corresponding images. For zero and positive time delays, the pump-only signal seen at -250 fs delay has been subtracted. Reprinted with permission from [57]. Copyright 2011, American Chemical Society.

initially excited droplet states that stretches from ~ 0.2 to ~ 2 eV evolves into three distinct spectral features within less than 1 ps. The features exhibit maxima near 0 eV ('ZEKE'), ≤ 0.1 eV ('B'), and ~ 0.7 eV ('A') as illustrated in Figure 10(b), which shows selected KE spectra at delays $\Delta t = 0$ fs (dark grey area), 200 fs (dashed), and 5–9 ps (solid).

A detailed analysis of the time-dependent intensities and photoelectron angular distributions (PADs) shows that signals A and B are predominantly associated with the emergence of free Rydberg atoms in $1s4p$ and $1s3d$ states, respectively, on timescales < 100 and 200 fs. The different appearance times of fragments with different principal quantum numbers n (and the observation that the $1s4p$ fragments are electronically aligned with respect to the pump laser polarisation while the $1s3d$ fragments are not) are consistent with a picture in which the $n = 4$ atoms are ejected predominantly from the very outermost surface of the droplets while the $n = 3$ fragments emerge from deeper regions and are, therefore, subject to more extended interactions with the surrounding helium bath. Note that, in particular, the energies of isolated atomic $n = 3$ states are outside the bandwidth of the pump pulse and, therefore, can only emerge through relaxation from higher lying droplet states [57]. The correlation of the $1s4p$ atoms with droplet relaxation has been confirmed by ion imaging experiments (see below) and a control experiment, in which the HH light passes through a helium gas cell before interacting with the target. For atomic He targets, HH absorption at the atomic He resonances in the cell prior to HH-target interaction led to an $\sim 90\%$ reduction in pump–probe signal associated with ionisation of $1s4p$ states while the corresponding signal emerging from helium droplets remained unchanged [93].

A schematic illustration of the emerging picture is given in Figure 11. The average particle density in large helium nanodroplets increases with increasing depth from near isolated atom densities in the very outermost surface region to bulk liquid helium densities inside the droplet. In a simplified picture of localised, atomic-like states, excitation energies increase accordingly with increasing depth starting from approximately isolated atom values at the surface to strongly (~ 1 eV) blue-shifted values in the bulk. This depth-dependent energy landscape leads to the predominant excitation of $n = 4$ states at the outermost surface and $n = 3$ states in deeper surface regions when the pump photon energies are in the vicinity of the $1s4p \leftarrow 1s^2$ resonance of isolated He atoms. The downhill energy gradient from inner to outer surface regions results in an outward radial force that leads to the ejection of Rydberg fragments (white arrows). This force provides a likely explanation for the observation of free Rydberg atom

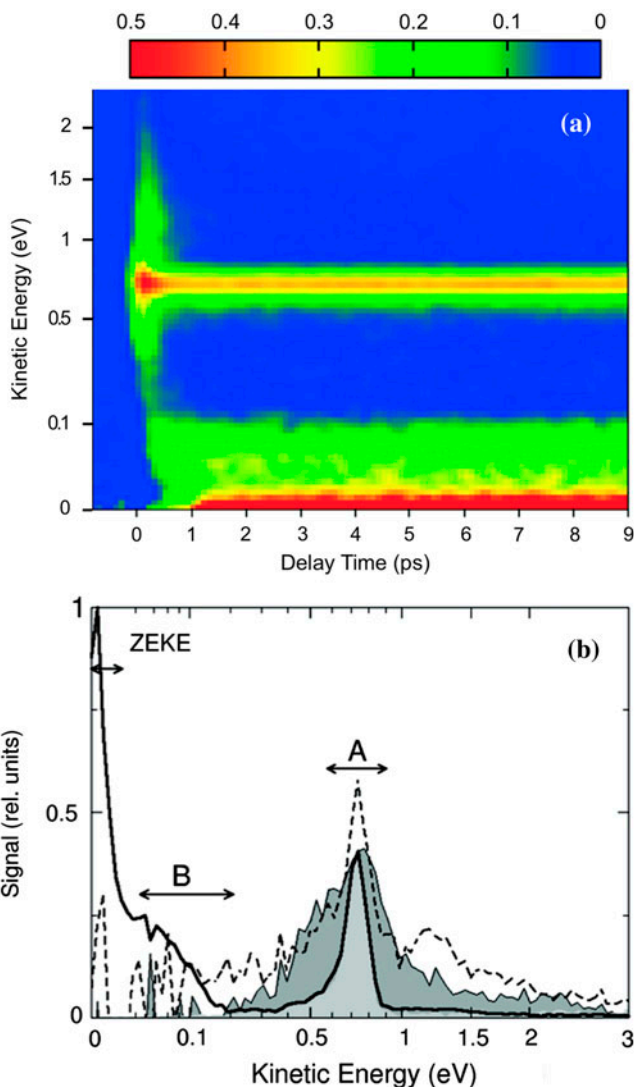


Figure 10. (a) Femtosecond time-resolved photoelectron KE distributions for excitation with 23.7 eV and ionisation with 1.6 eV photons. (b) Selected energy spectra at $\Delta t = 0$ fs (dark grey area), 200 fs (dashed), and 5–9 ps (solid). Note the nonlinear energy scale. Adapted with permission from [57]. Copyright 2011, American Chemical Society.

relaxation lines in the dispersed fluorescence measurements by von Haeften *et al.* [78]. As with the conduction band edge discussed in Sections 1 and 5, the effect is driven by electron confinement by neighbouring ground state helium atoms and the potential energy available for fragment ejection is governed by the difference between the pump photon energy and the asymptotic energies of the isolated Rydberg fragments. The substantial interaction of the $n = 3$ atoms with surrounding helium on their way out of the droplet leads to the loss of the initial electronic alignment and an increase of the predominant angular momentum from the dipole-allowed p states, which are expected to

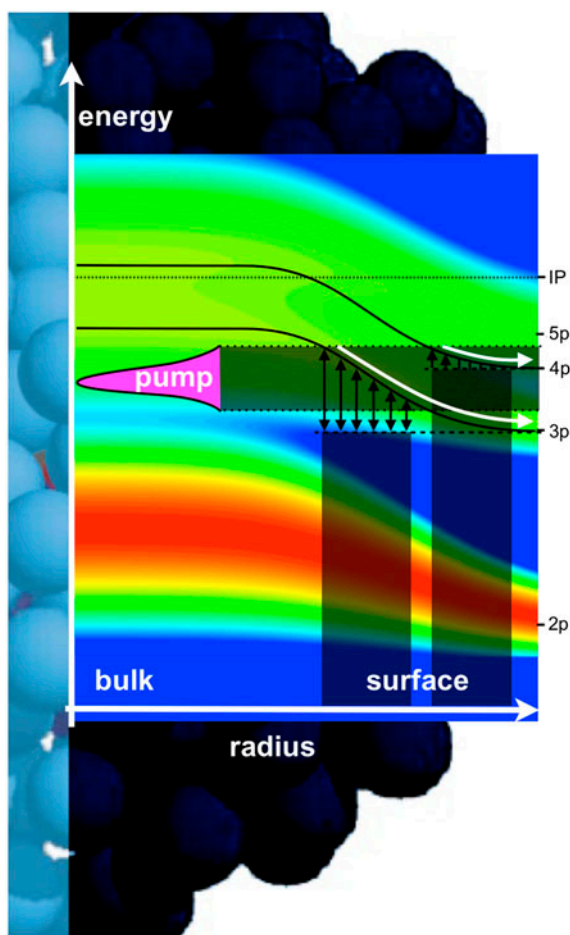


Figure 11. Schematic of band structure and Rydberg atom ejection trends near the surface of large ($\langle N \rangle \sim 10^6$) helium nanodroplets. The average particle density increases from near isolated atom densities in the very outermost surface region to bulk liquid helium densities inside the droplet. Excitation energies of localised, atomic-like states increase with depth starting from approximately isolated atom values at the surface to strongly (~ 1 eV) blue-shifted values in the bulk. The downhill energy gradient from inner to outer surface regions results in an outward radial force that leads to the ejection of Rydberg fragments.

be excited by the pump pulse, to d states of the ejected $n = 3$ fragments. While this result from the time-resolved PADs is consistent with the findings of the Möller group achieved by visible fluorescence measurements [78], a conclusive theoretical model for the preferential angular momentum $l = 2$ of the ejected monomers is still to be derived.

The validity of the model for the ejection of Rydberg atoms described above has been carefully tested in a series of femtosecond time-resolved ion imaging experiments. Using essentially the same droplet generation and pump–probe conditions as in the transient PAD experiments ($\langle N \rangle = 2 \times 10^6$, $h\nu_{\text{pump}} = 23.6$ eV, $h\nu_{\text{probe}} = 1.6$ eV), transient KEs of mass-resolved ions were recorded as described in Section 3. Figure 12 shows the results for He^* monomers ejected by electronically excited droplets [59].

Ionisation of these fragments by the probe pulse results in the time-dependent total yield of He^+ monomer ions shown in Figure 12(a). The measured intensities (black) are well described by a two-component fit (grey) comprising the same signal rise times as found in the transient photoelectron imaging experiments. This strongly suggests that the fast (<100 fs) rising monomer ion contribution (red) is associated with 1s4p fragments and the slower (~ 200 fs, green) appearing ions with 1s3d fragments as indicated by the red and green labels, respectively, in Figure 12(a). The more crucial observation, however, with respect to the Rydberg atom ejection model is derived from the transient monomer ion KE distributions shown in Figure 12(b). The transient KE spectra can be consistently described by a two-dimensional fit (Figure 12(c)) that employs the two components shown in Figure 12(a) and only varies their relative intensities across different ion KEs. This procedure corresponds to the assumption that the two product channels are associated with well defined, constant KE distributions and only their relative contributions change over time. The corresponding KE spectra of the two components are shown in Figure 12(d) using the same colour scheme as in Figure 12(a). Note the logarithmic intensity scales in (b), (c), and (d) that emphasise the excellent fit quality. The central finding is that, in agreement with the He^* ejection model sketched in Figure 11, the 1s3d fragments pick up higher kinetic energies on their way through the droplet surface than the 1s4p fragments due to the larger energy difference between the pump photon energy and the asymptotic energies of the isolated atoms, i.e. the larger blue-shift of the $n = 3$ excitations in the deeper surface regions compared to the small blue shifts of the $n = 4$ excitations at the outermost surface.

While Figure 11 and the discussion above give a qualitative impression of the density gradient ejection model, our group has also provided quantitative support for its validity as illustrated in Figure 12(e) and (f). The measured ion KE spectra (black) of the 1s4p (e) and 1s3d (f) fragments are compared to the results of a Monte-Carlo simulation (blue) of the fragment trajectories by Bünemann *et al.* [59], which is based on depth dependent potential energy surfaces calculated by Kornilov *et al.* [57]. The simulation clearly reproduces the dominant trends of the Rydberg atom ejection energetics. In particular, the substantial difference in the KEs for different principal quantum numbers is well described. We note that there are no adjustable parameters in the simulation, which is based on the experimentally derived density profile of large He droplets [8], the measured pump photon spectrum, and a simple hard-sphere scattering model to include the interaction of the ejected Rydberg atoms with surrounding ground state He atoms. The impact of this interaction on the ejection energies is illustrated by the grey, dashed lines in Figure 12(e) and (f). These curves have been derived by the same Monte-Carlo simulation as the blue lines but without inclusion of scattering. While neglecting the impact of scattering leads to a relatively minor deviation from the experiment for the 1s4p fragments, it shifts the centre energy of the dominant 1s3d fragment KE peak to approximately double the measured value. This is consistent with the key assumption of the model that the $n = 3$ fragments emerge from deeper regions of the droplet surface than the $n = 4$ fragments and, therefore, undergo more extended interactions with the surrounding ground state atoms.

The appearance time of the 1s3d fragments (~ 200 fs, Figures 10(a) and 12(a)) is, within the experimental uncertainty, identical to the relaxation time of the initially excited droplet states (Figure 10(a)). This observation indicates that the excited droplet signal and the emerging Rydberg signals are directly correlated and, based on the discussion of the ejection model, emerge from processes proceeding within the surface region of the probed droplets. Note that this does not exclude bulk excitations by the

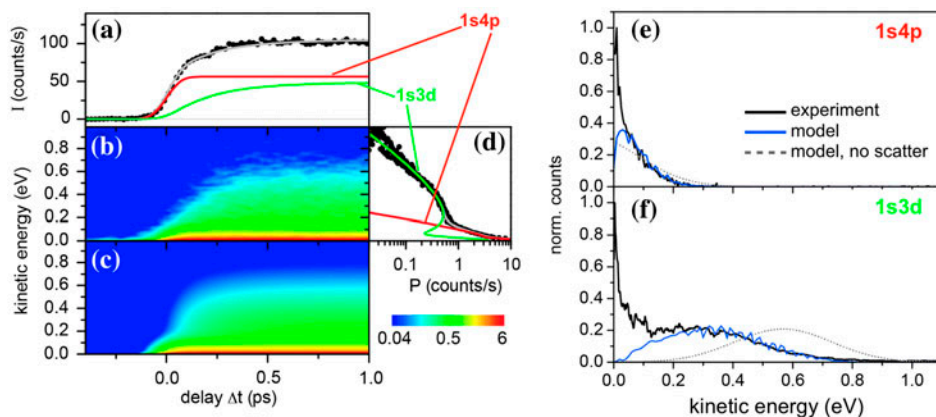


Figure 12. He^+ KE distributions following pump-probe photoionisation of large ($\langle N \rangle = 2 \times 10^6$) helium nanodroplets. (a) Time-dependent total He^+ yield (black) described by a two-component fit (grey). Red and green curves are the two fit components rising within < 100 and ~ 200 fs, respectively, corresponding to ionisation of 1s4p and 1s3d Rydberg fragments by the probe pulse. (b) Measured time-resolved ion KE distributions, which are modelled by a two-dimensional fit in (c). The fit adjusts the relative contributions of the two components shown in (a) for all kinetic energies, resulting in the KE spectra shown in (d). Note the logarithmic intensity scales in (b), (c), and (d) that emphasise the excellent fit quality. (e) and (f) compare the measured KE spectra (black) of the 1s4p and 1s3d fragments, respectively, with the results of a Monte-Carlo simulation (blue) of ion trajectories in the droplet surface region. Adapted with permission from [59] Copyright 2012, AIP Publishing LLC.

23.7 eV pump photons, but the 1.6 eV probe photons seem to directly ionise either states within the droplet's surface region or isolated Rydberg fragments. This conclusion will be extended by bulk-sensitive probing with 3.2 eV photons in the following sections.

7. Dynamics within the droplet bulk

The diameter of a droplet containing an average number of $\langle N \rangle = 2 \times 10^6$ atoms is approximately 55 nm [26]. The thickness of the surface region within which the particle density drops from 90 to 10% of the bulk value is only $\sim 6\text{--}8$ Å [8]. Therefore, fewer than 5% of all atoms are located in the droplet surface region where the dynamics discussed in the previous section take place. This indicates that substantially more atoms should be excited in the droplet bulk than in the surface region. The ZEKE signal in Figure 10 indicates the possibility of excitations other than those leading to Rydberg ejection, which will be discussed in more detail in Section 8. All other signals presented in Figures 10 and 12 likely emerge from the droplet surface or ejected fragments, including the photoelectron signals from the initially excited droplet states, whose decay nicely matches the rise of the ejected 1s3d Rydberg atoms. Given the above estimates and previous experimental evidence for bulk excitations beyond 23 eV [69], a likely explanation for the absence of any further evidence of bulk processes in the data presented thus far most likely lies in a lack of sensitivity of the experimental scheme to probe them. This is indeed confirmed by a more recent series of femtosecond time-resolved photoelectron imaging experiments using higher probe photon energies [60].

Figure 13(a) shows femtosecond time-resolved photoelectron velocity map images (after BASEX transformation) for pump- and probe-photon energies of 23.7 and 3.2 eV, respectively. Converting the VMI images to transient photoelectron KE distributions results in Figure 13(b). Evidently, most dynamic trends are dramatically different from those observed with 1.6 eV probe photons (Figures 9 and 10). Note that all KEs in Figure 13 are expected to be shifted to higher values by 1.6 eV compared to Figure 10 due to the difference in probe photon energies. Thus, the signal associated with the initially excited droplet states that peaks at ~ 0.7 eV in Figure 10, appears at ~ 2.3 eV in Figure 13(b). Apart from this initial energetically broad and quickly-decaying photoelectron signal, however, there is virtually no resemblance between the KE distributions recorded with 1.6 and 3.2 eV photons. In particular, the energetically narrow Rydberg fragment signals that dominate Figure 10(a) are essentially absent from Figure 13. While the photoionisation cross sections of ejected Rydberg atoms are expected to drop significantly with increasing probe photon energy [72], oscillator strength arguments are not sufficient to explain the complete loss of Rydberg signals in the measurements with 3.2 eV probe photons. Instead, it is very likely that these

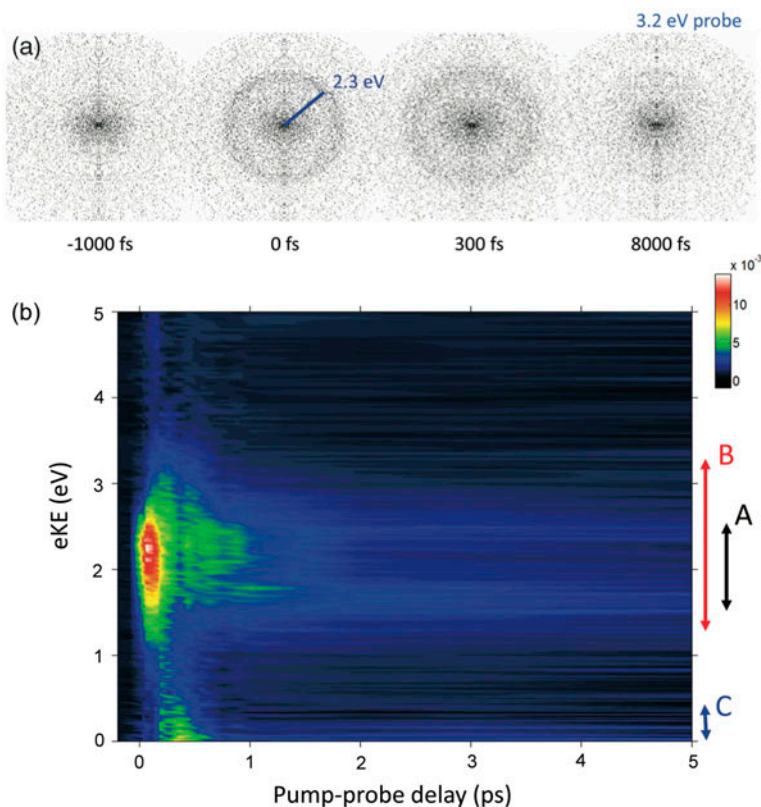


Figure 13. (a) Time-resolved photoelectron velocity map images (after BASEX transformation) for pump- and probe-photon energies of 23.7 and 3.2 eV, respectively. For reference, the blue line shows the radius of a ring corresponding to an electron KE = 2.3 eV. (b) Time-resolved photoelectron KE distributions derived from the VMI images. Reprinted with permission from [60]. Copyright 2014, AIP Publishing LLC.

experiments are predominantly probing electronic dynamics proceeding in the droplet bulk and traces of the surface dynamics such as Rydberg atom ejection are simply overwhelmed by a much stronger bulk response.

One argument for this picture draws from the suppression of electrons with less than ~ 1 eV KE emerging from Penning ionisation of dopants inside large He droplets, as seen in Figure 7 and discussed in Section 5 [90]. Similar to slow electrons from indirect dopant ionisation, photoelectrons generated by 1.6 eV probe photons inside the droplet bulk can, for the most part, not overcome a 1 eV barrier since the total pump + probe photon energy (~ 25.3 eV) lies only ~ 0.7 – 0.8 eV above the threshold for direct droplet ionisation and, therefore, below the conduction band onset. With 3.2 eV photons, however, photoemission from the bulk becomes possible.

The pump–probe delay dependent photoelectron KE distributions in Figure 14(a) (data identical to Figure 13(b)) are described by a model that employs three components corresponding to three constant KE spectra with time-dependent intensities. Both the spectra and the dynamic timescales are derived simultaneously in a two-dimensional nonlinear least-squares fit procedure, leading to the model function shown in Figure 14(b) [60]. The KE spectra of the three components are displayed in Figure 14(c), and their time-dependent intensities are shown in Figure 14(d) using identical colour codes. Note that all components in Figure 14(c) are scaled to the same maximum while their relative contributions can be seen in Figure 14(d). Most of the detected photoelectron signal is described by a combination of two components.

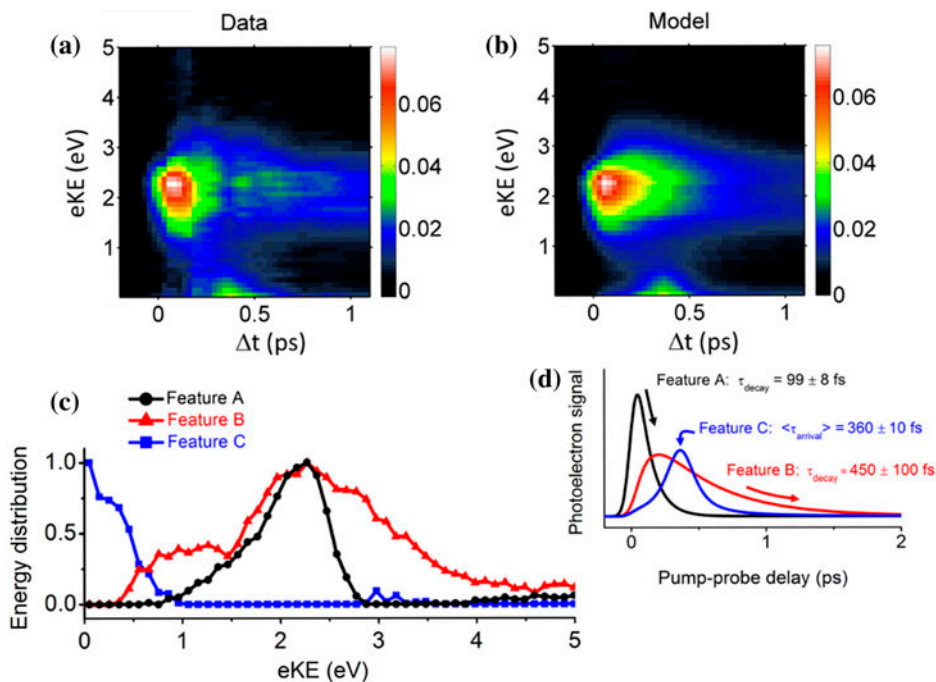


Figure 14. Global fit of time-resolved photoelectron spectra with 3.2 eV probe photons. Shown are (a) raw data, (b) the best fit model, and (c) extracted energy distributions for the three fit components (normalised to the same maximum intensity). (d) Time-dependent intensities of the three dynamical components. Reprinted with permission from [60]. Copyright 2014, AIP Publishing LLC.

An ~ 1 eV broad photoelectron band that peaks at ~ 2.3 eV appears instantly and decays within ~ 100 fs. (black curves, Feature A). A second photoemission band peaks at the same energy as the first one but is much broader in energy and its delayed rise is commensurate with the decay time of the first component before it also decays within approximately 0.5 ps (red curves, Feature B). The third component (blue) will be discussed in Section 8.

The peak position and shape of the instantly rising component is compatible with the signal from initially excited droplet states in Figure 10(b) (dark grey area), only shifted by 1.6 eV to higher photon energies. It is, therefore, also assigned to photoemission from states that are directly accessed by the pump pulse. However, the signal that emerges in sync with the decay of the initial droplet states is much broader than any other photoelectron bands and, in particular, extends to very high KEs beyond the probe photon energy of 3.2 eV. Evidently, the ionic states accessed by these photoionisation events must be marked by potential energies well below the vertical droplet IP. In fact, the difference between the total pump + probe photon energy (~ 26.9 eV) and the high-energy cutoff of the transient photoelectron Feature B (~ 4 eV) matches the previously determined adiabatic IP of large helium droplets as discussed in Section 5 (~ 23 eV). Ionic droplet states below the vertical IP are associated with the formation of dimers and larger clusters, which have lower IPs than isolated or weakly interacting helium atoms due to attractive interactions at short internuclear distances [63–65]. The emergence and decay of Feature B is, therefore, assigned to the formation and subsequent relaxation and/or dissociation of He molecules and clusters that are at least transiently marked by shorter internuclear distances than the ground state He droplet. Based on the direct correlation between the appearance of the molecular signals and the initially excited droplet state decay, the short lifetimes of the transiently populated molecular configurations, and the lack of any signals associated with surface processes, the observed dynamics are associated with processes inside the bulk of the droplets.

8. Interband relaxation

Rydberg fragment ejection as described in Section 6 was long believed to be the predominant relaxation pathway of neutral helium nanodroplets after excitation beyond 23 eV. Fluorescence and autoionisation were considered the only alternatives albeit with significantly lower probability. The results presented in Figures 13 and 14 reveal an additional relaxation channel that, to the best of our knowledge, had never been described prior to the implementation of ultrafast EUV probing techniques. The intense peak (Feature C) appearing within ~ 360 fs at KEs below ~ 1 eV is a clear indication that a significant fraction of droplets excited into the 1s3p/4p band undergo interband relaxation to the 1s2p band [60]. The KE spectrum of the new transient feature (blue curve in Figure 14(c)) mimics the high-energy side of the 1s2p band in Figure 3, which can be projected onto the ionic continuum by the 3.2 eV probe pulse. Based on the fact that no indications for this interband transition were detected by fluorescence measurements and the description of the bulk dynamics in Section 7, the new relaxation channel is most likely associated with radiationless transitions mediated by coupled electronic–nuclear dynamics involving two or more atoms. Moreover, the significant intensity of the 1s2p band photoelectron signal compared to that of the initially populated 1s3p/4p band indicates that these interband transitions take place predominantly inside the droplet bulk.

Interestingly, the relaxation products themselves are transient, decaying rather quickly after peaking in intensity approximately 360 fs after the EUV excitation. This is likely due to intraband cooling within the 1s2p band and, possibly, further relaxation to 1s2s states. Both processes appear as possible relaxation pathways in molecular dynamics (MD) simulations [81] and are currently investigated at the FERMI FEL, where a 4.8 eV probe laser is employed that is capable of ionising the entire 1s2p band range [94]. A possible influence of other mechanisms such as bubble formation cannot be excluded at this stage.

The discovery of the interband relaxation channel is an illustrative example for the particular strength of time-domain techniques to detect intermediates that are challenging to observe with time-averaged probes. In fact, in addition to the short relaxation timescale observed with 3.2 eV probe pulses, another transient signal from the experiments using 1.6 eV probe photons indicates that interband transitions are the dominant relaxation channel of bulk excitations in large He droplets beyond 23 eV. Figure 15 shows the time-dependent intensity of the ZEKE photoelectron signal in Figure 10 recorded with pump- and probe-photon energies of 23.7 and 1.6 eV, respectively. The transient ZEKE intensities are given relative to the ZEKE signal induced by the pump pulse alone, which is assigned an intensity of 1. The inset shows a more detailed study of the region near zero pump-probe delay.

Initially, probe-pulse induced direct ionisation diminishes the population of neutral droplet states undergoing autoionisation, leading to a depletion of the ZEKE signal at pump-probe delays $\Delta t < 300$ fs. At longer times, however, interaction of the droplets with the probe pulse leads to a significant, up to ~50% enhancement of the ZEKE production. A likely explanation for this trend is that most of the initially excited droplets relax from the 1s3p/4p band down to the $n = 2$ band(s) from where they can be re-excited to the $n = 3,4$ band by the 1.6 eV probe photons and, therefore, produce

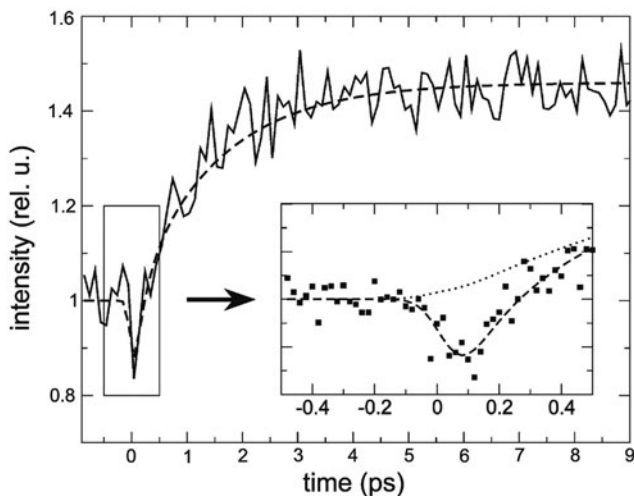


Figure 15. Intensity of the ZEKE photoelectron signal as a function of pump-probe delay for pump and probe photon energies of 23.7 and 1.6 eV, respectively. The inset shows a more detailed study of the region near zero pump-probe delay, demonstrating a transient signal depletion before its intensity overshoots the pump-only value. Reprinted with permission from [57]. Copyright 2011, American Chemical Society.

additional ZEKE electrons through autoionisation [56,57]. Given that the absorption probability for a probe photon is significantly less than 100% (otherwise multi-photon effects would become apparent), a ZEKE signal enhancement of 50% corresponds to an overwhelming fraction of droplets undergoing interband relaxation compared to any other de-excitation channel. By the same line of argumentation, the result confirms that autoionisation producing ZEKE electrons is indeed a minor relaxation pathway. The fast recovery of the ZEKE signal in Figure 15 within a few hundred femtoseconds is consistent with the fast relaxation timescales illustrated in Figures 13 and 14. The picosecond timescale of the continued ZEKE growth, however, has no direct complement in the other photoelectron signals. It may be related to continued relaxation within the $n = 2$ droplet state manifold and/or other dynamics affecting the re-excitation probability by the probe photon through Franck-Condon factors and/or selection rules.

The absence of the ZEKE overshoot in Figure 13 is an indirect confirmation of the interband relaxation/re-excitation picture since 3.2 eV probe photons are largely incompatible with the droplet band gap (Figure 3). We note, however, that the transient intensities of ejected Rydberg molecules, which will be discussed in more detail in the following section, are partially marked by similar appearance times as the ZEKE overshoot.

9. Ejection of molecular species from droplets

As discussed in Section 4, the fluorescence action spectra of pure He droplets show evidence for emission from electronically excited He_2^* fragments that are ejected from the droplet subsequent to EUV excitation [78]. This observation raises the issue of whether the ejection of various molecular fragments from pure droplets can be time-resolved, and whether the fragments can be identified and characterised. Time-resolved measurements in alkali-doped helium droplets by the Stienkemeier and Scoles groups have focused on the formation of exciplexes between helium and alkali atoms initially adsorbed on the droplet surface [29,30,95–101]. Depending on the alkali atom used, the timescale for this process varies from hundreds of fs to the ps regime, meaning that it competes with the other relaxation channels discussed so far in this review [97,98].

For pure droplets, the time-dependent photoelectron signals alone do not exhibit obvious signatures of molecular fragment ejection. However, the time-dependent ion imaging signals shown in Figure 16 show clear evidence for this process [59]. The results in Figure 16 were obtained at pump and probe photon energies of 23.6 and 1.6 eV, respectively. The time-dependent ion mass spectra shown in Figure 16(a) consist almost entirely of He^+ , He_2^+ , and He_3^+ ions, with the trimer ions accounting for less than 5% of the total ion signal. Figure 16(b) shows the time-dependent signals for these three ions normalised to their values at 10 ps. While the He^+ ion signal, discussed in more detail in Section 6, rises to its asymptotic value within less than 0.5 ps, the other two ions exhibit more complex dynamics. Both rise instantaneously, then exhibit a fast decay within 200 fs and a subsequent rise on a 2–3 ps timescale.

Time-dependent ion-imaging signals for He_2^+ and He_3^+ were analysed similarly to those for He^+ as shown in Figure 12(a)–(d); results for He_2^+ are shown in Figure 17. This more detailed analysis shows that the He_2^+ signal comprises three components, each with a different KE distribution: an instantaneously rising component (D1) that decays within 200 fs, and two components that rise with time constants of 200 fs and 2.5 ps (D2 and D3). For He_3^+ (not shown), only the first and third components were observed.

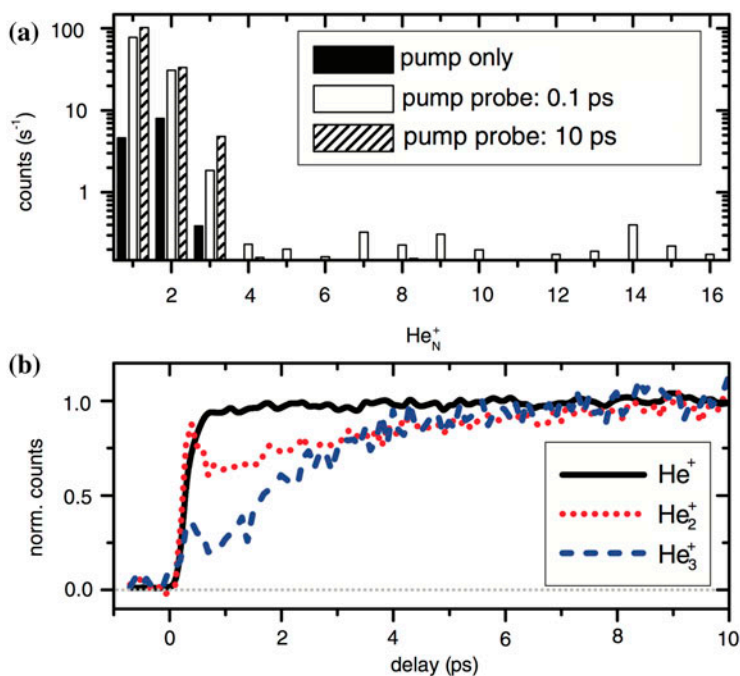


Figure 16. (a) Time-resolved photo-cation distributions for pump-probe ionisation of helium droplets with excitation in the $1s3p/4p$ band and ionisation at 1.6 eV. (b) Ion yields for He^+ , He_2^+ and He_3^+ as a function of pump-probe delay. Reprinted with permission from [59]. Copyright 2012, AIP Publishing LLC.

The molecular ion signals can arise either from probe-ionisation of neutral Rydberg molecular fragments (i.e. He_2^*) ejected by the droplet, or from ions generated within the droplet by the pump and probe pulses that are then ejected as molecular ions. It is likely that D2 results from He_2^* ejected from the droplet and ionised by the probe, given the similarity in dynamics to the $\text{He}^*(n=3)$ signal in Figure 12. D1, which decays on a 200 fs timescale, may be from ionisation of Rydberg atoms at the droplet surface, followed by ejection of He_2^+ and He_3^+ fragments. The slowest rise time, 2.5 ps, matches that seen for the ZEKE electrons in Figure 15. Since the ZEKE electron signal most likely arises from autoionisation within the droplet, the slowly rising components of the He_2^+ and He_3^+ signals may, therefore, correspond to ionic species whose formation accompanies autoionisation.

While the femtosecond time-resolved yields and KE distributions of the molecular fragments exhibit distinct connections to the photoelectron dynamics as described above, no simple picture has yet emerged in order to model their dynamics in a similar fashion as performed for the monomer fragments. Nevertheless, the results clearly demonstrate the emergence of excited molecular fragments from electronically excited helium nanodroplets on femtosecond to picosecond timescales. Associative interactions between atoms in electronically excited droplets are also a likely source for the significant deviations between measured and modelled ion KE distributions at very small KE values (Figure 12(e) and (f)). Attractive atom-atom forces are not taken into account in the hard sphere scattering that is entirely based on repulsive interactions. While a predictive description of the entire Rydberg ejection manifold of large helium droplets is

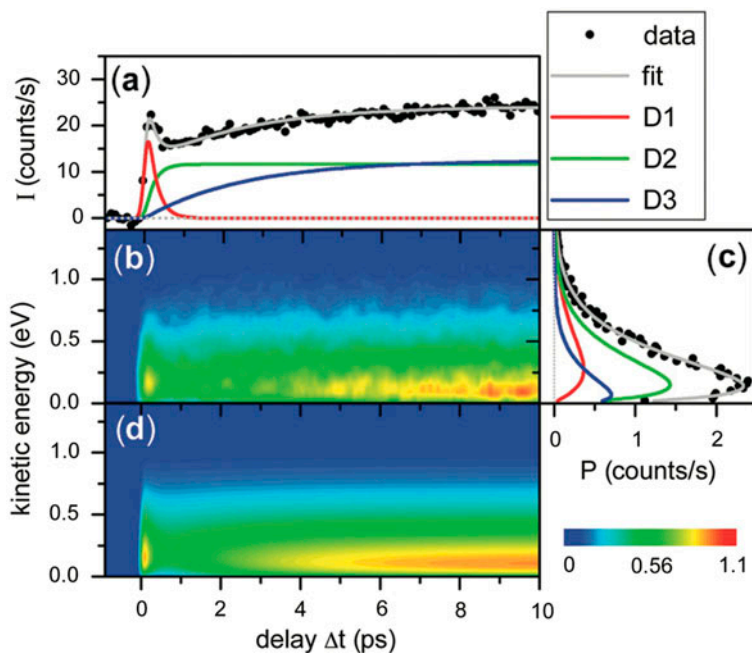


Figure 17. He_2^+ KE distributions following pump-probe photoionisation of large ($\langle N \rangle = 2 \times 10^6$) helium nanodroplets. (a) Time-resolved He_2^+ yield (black) decomposed into a three component least squares fit. (b) He_2^+ emission as a function of time and product KE. (c) KE distributions for data (black) and model (grey) composed of the same three components (red, green, blue) as indicated in (a). (d) Best global 2D fit model. Reprinted with permission from [59]. Copyright 2012, AIP Publishing LLC.

beyond the reach of currently available theoretical models, very recent *ab initio* MD simulations by Closser and coworkers for 7-atom helium clusters indicate that some trends, including the ejection of very slow fragments and the formation of dimers and trimers, are already reproduced by state-of-the art models of comparably small systems [81].

For 100 randomised 7-atom configurations, excitation into the $1s2s/2p$ state manifold and subsequent relaxation has been described by combining *ab initio* based electron configurations with classical propagation of the atomic cores on the corresponding electronic potential energy surfaces. Dynamics at surface crossings are modelled by letting a system continue to propagate beyond a crossing based on the best wavefunction overlap between previous and successive time steps. Figure 18 illustrates a specific trajectory of the MD simulations. White spheres mark the time-dependent positions of the atomic cores. The electronic dynamics are represented as transient detachment (red) and attachment (blue) distributions that represent the change in electron densities relative to the cluster's neutral ground state. The particular relaxation pathway shown here is marked by a fairly delocalized initial excitation (Figure 18(a)) that quickly localises within ≈ 120 fs around two atoms, which are eventually expelled as an excited, bound dimer. The 7-atom model is of course not representative of the large helium droplets studied in the experiments. Nevertheless, the appearance of molecular complexes in both experiment and theory on similar timescales [81] is very encouraging for efforts to push the realm of the MD simulations toward larger systems.

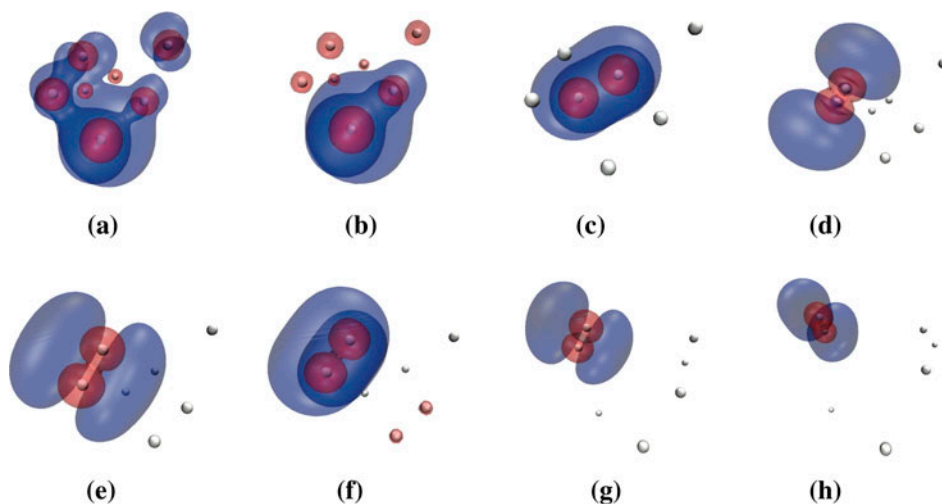


Figure 18. Results of an *ab initio* MD simulation. Shown are the calculated electron attachment (blue)/detachment (red) densities for a dimer-forming trajectory originating in the $1s2p$ manifold of a 7 atom system. Figures correspond to time delays of (a) $t = 0$ fs, (b) $t = 121$ fs, (c) $t = 242$ fs, (d) $t = 302.5$ fs, (e) $t = 363$ fs, (f) $t = 423.5$ fs, (g) $t = 726$ fs, and (h) $t = 968$ fs after excitation. White spheres indicate the positions of the atomic cores. Reprinted with permission from [81]. Copyright 2012, AIP Publishing LLC.

10. Summary and prospects

Superfluid helium nanodroplets continue to attract attention across a growing number of scientific communities. More than two decades after the first experimental characterisation of their electronically excited states, many questions remain regarding the microscopic nature of the electronic excitations in the quantum liquid. The combination of increasingly powerful energy- and time-domain experiments with state-of-the-art *ab initio* electronic structure calculations and MD simulations has provided a wealth of information on the droplets' electronic structure and possible relaxation pathways. Many findings are beginning to form a consistent picture, while others highlight the need for further experimental and theoretical work.

A general consensus has emerged that the blue-shift and broad nature of the droplet bands relative to the atomic helium absorption lines may be described within a picture of fairly localised electronic excitations. In the droplet surface region, in particular, these excitations give rise to fast ejection of atomic and molecular fragments, partly with significant kinetic energies. While experimental and theoretical findings for excitations and dynamics in the surface regions converge to a fairly comprehensive picture, our understanding of corresponding processes inside the bulk of large helium droplets is much less complete. At least five different relaxation mechanisms have been tentatively identified with bulk excitations. Beside autoionisation to produce ZEKE electrons, interband relaxation, and the formation of transient, excited molecular complexes inside the droplets discussed here in more detail, bubble formation and fluorescence decay remain likely alternatives that have so far been characterised only to a very limited degree in the time-domain. The narrow bandwidth and continuous tunability of EUV FELs offer particularly exciting new opportunities to study the competition and

correlation between multiple surface- and bulk-relaxation channels and first efforts have been launched to exploit these opportunities.

Another frontier that has been touched on only briefly herein is the study of energy- and charge-migration within doped helium nanodroplets. Energy-domain studies have provided a number of exciting findings indicating a variety of pathways to transfer energy and charge between the helium matrix and dopant atoms. In these experiments, the droplet effectively acts as an EUV chromophore that couples very efficiently to the electronic degrees of freedom of the deposited species, multiplying the efficiency of the light-dopant interaction. Time-domain experiments using both HHG and FEL based ultrashort EUV pulses are well positioned to gain a deeper insight into the underlying mechanisms.

Disclosure statement

No potential conflict of interest was reported by the authors.

Funding

This work was supported by the U.S. Department of Energy, Office of Basic Energy Sciences, Chemical Sciences, Geosciences and Biosciences Division, through Contract No. DEAC02-05CH11231.

ORCID

Oliver Gessner  <http://orcid.org/0000-0003-4709-2822>

References

- [1] A. Einstein, Sitzber. Preuss. Akad. Wiss. **3**, 261 (1924).
- [2] A.F. Borghesani, *Ions and Electrons in Liquid Helium* (Oxford University Press, Oxford, 2007).
- [3] S. Grebenev, J.P. Toennies, and A.F. Vilesov, *Science* **279**, 2083 (1998).
- [4] L.F. Gomez, K.R. Ferguson, J.P. Cryan, C. Bacellar, R.M.P. Tanyag, C. Jones, S. Schorb, D. Anielski, A. Belkacem, C. Bernando, R. Boll, J. Bozek, S. Carron, G. Chen, T. Delmas, L. Englert, S.W. Epp, B. Erk, L. Foucar, R. Hartmann, A. Hexemer, M. Huth, J. Kwok, S.R. Leone, J.H.S. Ma, F.R.N.C. Maia, E. Malmerberg, S. Marchesini, D.M. Neumark, B. Poon, J. Prell, D. Rolles, B. Rudek, A. Rudenko, M. Seifrid, K.R. Siefermann, F.P. Sturm, M. Swiggers, J. Ullrich, F. Weise, P. Zwart, C. Bostedt, O. Gessner, and A.F. Vilesov, *Science* **345**, 906 (2014).
- [5] J.K. Badenhop and F. Weinhold, *J. Chem. Phys.* **107**, 5422 (1997).
- [6] N. Ashcroft, *Physica* **35**, 148 (1967).
- [7] R. Grisenti, W. Schöllkopf, J. Toennies, G. Hegerfeldt, T. Köhler, and M. Stoll, *Phys. Rev. Lett.* **85**, 2284 (2000).
- [8] J. Harms, J.P. Toennies, and F. Dalfovo, *Phys. Rev. B* **58**, 3341 (1998).
- [9] S. Stringari and J. Treiner, *J. Chem. Phys.* **87**, 5021 (1987).
- [10] K. Tang and J. Toennies, *J. Chem. Phys.* **118**, 4976 (2003).
- [11] K. Tang, J. Toennies, and C. Yiu, *Phys. Rev. Lett.* **74**, 1546 (1995).
- [12] J. Jortner, N.R. Kestner, S.A. Rice, and M.H. Cohen, *J. Chem. Phys.* **43**, 2614 (1965).
- [13] U. Asaf and I. Steinberger, *Chem. Phys. Lett.* **128**, 91 (1986).

- [14] M.A. Woolf and G. Rayfield, *Phys. Rev. Lett.* **15**, 235 (1965).
- [15] L. Bruschi, B. Maraviglia, and F. Moss, *Phys. Rev. Lett.* **17**, 682 (1966).
- [16] W. Schoepe and C. Probst, *Phys. Lett. A* **31**, 490 (1970).
- [17] W. Sommer, *Phys. Rev. Lett.* **12**, 271 (1964).
- [18] K.D. Closser and M. Head-Gordon, *J. Phys. Chem. A* **114**, 8023 (2010).
- [19] J.R. Broomall, W.D. Johnson, and D.G. Onn, *Phys. Rev. B* **14**, 2819 (1976).
- [20] C. Surko, G. Dick, F. Reif, and W. Walker, *Phys. Rev. Lett.* **23**, 842 (1969).
- [21] K. von Haefen, T. Laarmann, H. Wabnitz, and T. Möller, *Phys. Rev. Lett.* **88**, 233401 (2002).
- [22] J.P. Toennies and A.F. Vilesov, *Angew. Chem. Int. Edit.* **43**, 2622 (2004).
- [23] M. Mudrich and F. Stienkemeier, *Int. Rev. Phys. Chem.* **33**, 301 (2014).
- [24] S. Yang and A.M. Ellis, *Chem. Soc. Rev.* **42**, 472 (2013).
- [25] H. Buchenau, E. Knuth, J. Northby, J. Toennies, and C. Winkler, *J. Chem. Phys.* **92**, 6875 (1990).
- [26] L.F. Gomez, E. Loginov, R. Sliter, and A.F. Vilesov, *J. Chem. Phys.* **135**, 154201 (2011).
- [27] E. Knuth and U. Henne, *J. Chem. Phys.* **110**, 2664 (1999).
- [28] S. Goyal, D. Schutt, and G. Scoles, *Phys. Rev. Lett.* **69**, 933 (1992).
- [29] J.L. Persson, Q. Hui, Z.J. Jakubek, M. Nakamura, and M. Takami, *Phys. Rev. Lett.* **76**, 1501 (1996).
- [30] M. Mudrich, F. Stienkemeier, G. Droppelmann, P. Claas, and C.P. Schulz, *Phys. Rev. Lett.* **100**, 023401 (2008).
- [31] M. Choi, G. Doublerly, T. Falconer, W. Lewis, C. Lindsay, J. Merritt, P. Stiles, and R. Miller, *Int. Rev. Phys. Chem.* **25**, 15 (2006).
- [32] S. Grebnev, M. Hartmann, M. Havenith, B. Sartakov, J.P. Toennies, and A.F. Vilesov, *J. Chem. Phys.* **112**, 4485 (2000).
- [33] E. Loginov, D. Rossi, and M. Drabbels, *Phys. Rev. Lett.* **95**, 163401 (2005).
- [34] A. Scheidemann, B. Schilling, J. Toennies, and J. Northby, *Phys. B* **165–166**, 135 (1990).
- [35] F. Stienkemeier and A.F. Vilesov, *J. Chem. Phys.* **115**, 10119 (2001).
- [36] M. Wewer and F. Stienkemeier, *Phys. Rev. B* **67**, 125201 (2003).
- [37] M. Lewerenz, B. Schilling, and J. Toennies, *J. Chem. Phys.* **102**, 8191 (1995).
- [38] E. Loginov, L.F. Gomez, N. Chiang, A. Halder, N. Guggemos, V.V. Kresin, and A.F. Vilesov, *Phys. Rev. Lett.* **106**, 233401 (2011).
- [39] E. Lugovoj, J.P. Toennies, and A. Vilesov, *J. Chem. Phys.* **112**, 8217 (2000).
- [40] K. Nauta and R. Miller, *Science* **287**, 293 (2000).
- [41] K. Nauta and R.E. Miller, *Science* **283**, 1895 (1999).
- [42] V. Mozhayskiy, M.N. Slipchenko, V.K. Adamchuk, and A.F. Vilesov, *J. Chem. Phys.* **127**, 094701 (2007).
- [43] M. Hartmann, R. Miller, J. Toennies, and A. Vilesov, *Phys. Rev. Lett.* **75**, 1566 (1995).
- [44] F. Lackner, G. Krois, M. Theisen, M. Koch, and W. Ernst, *Phys. Chem. Chem. Phys.* **13**, 18781 (2011).
- [45] E. Loginov and M. Drabbels, *Phys. Rev. Lett.* **106**, 083401 (2011).
- [46] E. Loginov, C. Callegari, F. Ancilotto, and M. Drabbels, *J. Phys. Chem. A* **115**, 6779 (2011).
- [47] K. von Haefen, T. Laarmann, H. Wabnitz, T. Möller, and K. Fink, *J. Phys. Chem. A* **115**, 7316 (2011).
- [48] D.C. Morton, Q.X. Wu, and G.W.F. Drake, *Can. J. Phys.* **84**, 83 (2006).
- [49] M. Joppien, R. Kambach, and T. Möller, *Phys. Rev. Lett.* **71**, 2654 (1993).
- [50] H. Buchenau, J.P. Toennies, and J.A. Northby, *J. Chem. Phys.* **95**, 8134 (1991).
- [51] P. Bartl, S. Denifl, P. Scheier, and O. Echt, *Phys. Chem. Chem. Phys.* **15**, 16599 (2013).
- [52] S. Denifl, M. Stano, A. Stamatovic, P. Scheier, and T. Märk, *J. Chem. Phys.* **124**, 054320 (2006).
- [53] C. Kim, S. Yurgenson, C.-C. Hu, and J. Northby, *J. Low Temp. Phys.* **113**, 1097 (1998).
- [54] P.B. Corkum, *Phys. Rev. Lett.* **71**, 1994 (1993).

- [55] A. Stolow, A.E. Bragg, and D.M. Neumark, *Chem. Rev.* **104**, 1719 (2004).
- [56] O. Kornilov, C.C. Wang, O. Bünermann, A.T. Healy, M. Leonard, C. Peng, S.R. Leone, D.M. Neumark, and O. Gessner, *J. Phys. Chem. A* **114**, 1437 (2010).
- [57] O. Kornilov, O. Bünermann, D.J. Haxton, S.R. Leone, D.M. Neumark, and O. Gessner, *J. Phys. Chem. A* **115**, 7891 (2011).
- [58] O. Bünermann, O. Kornilov, S.R. Leone, D.M. Neumark, and O. Gessner, *J. Sel. Top. Quant. Electron.* **18**, 308 (2012).
- [59] O. Bünermann, O. Kornilov, D.J. Haxton, S.R. Leone, D.M. Neumark, and O. Gessner, *J. Chem. Phys.* **137**, 214302 (2012).
- [60] M.P. Ziemkiewicz, C. Bacellar, K.R. Siefertmann, S.R. Leone, D.M. Neumark, and O. Gessner, *J. Chem. Phys.* **141**, 174306 (2014).
- [61] S.R. Krishnan, L. Fechner, M. Kremer, V. Sharma, B. Fischer, N. Camus, J. Jha, M. Krishnamurthy, T. Pfeifer, R. Moshhammer, J. Ullrich, F. Stienkemeier, M. Mudrich, A. Mikaberidze, U. Saalman, and J.M. Rost, *Phys. Rev. Lett.* **107**, 173402 (2011).
- [62] O. Kornilov and J.P. Toennies, *Europhys. News* **38**, 22 (2007).
- [63] R. Fröchtenicht, U. Henne, J.P. Toennies, A. Ding, M. Fieber-Erdmann, and T. Drewello, *J. Chem. Phys.* **104**, 2548 (1996).
- [64] D.S. Peterka, A. Lindinger, L. Poisson, M. Ahmed, and D.M. Neumark, *Phys. Rev. Lett.* **91**, 043401 (2003).
- [65] D.S. Peterka, J.H. Kim, C.C. Wang, L. Poisson, and D.M. Neumark, *J. Phys. Chem. A* **111**, 7449 (2007).
- [66] A.T.J.B. Eppink and D.H. Parker, *Rev. Sci. Instrum.* **68**, 3477 (1997).
- [67] N.B. Brauer, S. Smolarek, E. Loginov, D. Mateo, A. Hernando, M. Pi, M. Barranco, W.J. Buma, and M. Drabbels, *Phys. Rev. Lett.* **111**, 153002 (2013).
- [68] D. Buchta, S. Krishnan, N. Brauer, M. Drabbels, P. O’Keeffe, M. Devetta, M. Di Fraia, C. Callegari, R. Richter, M. Coreno, K.C. Prince, F. Stienkemeier, J. Ullrich, R. Moshhammer, and M. Mudrich, *J. Chem. Phys.* **139**, 084301 (2013).
- [69] D. Buchta, S.R. Krishnan, N.B. Brauer, M. Drabbels, P. O’Keeffe, M. Devetta, M. Di Fraia, C. Callegari, R. Richter, M. Coreno, K.C. Prince, F. Stienkemeier, R. Moshhammer, and M. Mudrich, *J. Phys. Chem. A* **117**, 4394 (2013).
- [70] A. LaForge, M. Drabbels, N.B. Brauer, M. Coreno, M. Devetta, M. Di Fraia, P. Finetti, C. Grazioli, R. Katzy, V. Lyamayev, T. Mazza, M. Mudrich, P. O’Keeffe, Y. Ovcharenko, P. Piseri, O. Plekan, K.C. Prince, R. Richter, S. Stranges, C. Callegari, T. Möller, and F. Stienkemeier, *Sci. Rep.* **4**, 03621 (2014).
- [71] Y. Ovcharenko, V. Lyamayev, R. Katzy, M. Devetta, A. LaForge, P. O’Keeffe, O. Plekan, P. Finetti, M. Di Fraia, M. Mudrich, M. Krikunova, P. Piseri, M. Coreno, N.B. Brauer, T. Mazza, S. Stranges, C. Grazioli, R. Richter, K.C. Prince, M. Drabbels, C. Callegari, F. Stienkemeier, and T. Möller, *Phys. Rev. Lett.* **112**, 073401 (2014).
- [72] L.H. Haber, B. Doughty, and S.R. Leone, *Phys. Rev. A* **79**, 031401 (2009).
- [73] W. Wiley and I.H. McLaren, *Rev. Sci. Instrum.* **26**, 1150 (1955).
- [74] O. Jagutzki, A. Cerezo, A. Czasch, R. Dorner, M. Hattas, M. Huang, V. Mergel, U. Spillmann, K. Ullmann-Pfleger, T. Weber, H. Schmidt-Bocking, and G.D.W. Smith, *IEEE Trans. Nucl. Sci.* **49**, 2477 (2002).
- [75] V. Lyamayev, Y. Ovcharenko, R. Katzy, M. Devetta, L. Bruder, A. LaForge, M. Mudrich, U. Person, F. Stienkemeier, and M. Krikunova, *J. Phys. B* **46**, 164007 (2013).
- [76] C. Bostedt, J.D. Bozek, P.H. Bucksbaum, R.N. Coffee, J.B. Hastings, Z. Huang, R.W. Lee, S. Schorb, J.N. Corlett, P. Denes, P. Emma, R.W. Falcone, R.W. Schoenlein, G. Doumy, E.P. Kanter, B. Kraessig, S. Southworth, L. Young, L. Fang, M. Hoener, N. Berrah, C. Roedig, and L.F. DiMauro, *J. Phys. B* **46**, 164003 (2013).
- [77] K. von Haefen, T. Laarmann, H. Wabnitz, and T. Möller, *J. Phys. B* **38**, S373 (2005).
- [78] K. von Haefen, A.R.B. de Castro, M. Joppien, L. Moussavizadeh, R. von Pietrowski, and T. Möller, *Phys. Rev. Lett.* **78**, 4371 (1997).
- [79] T.L. Gilbert and A.C. Wahl, *J. Chem. Phys.* **55**, 5247 (1971).

- [80] S.L. Guberman and W.A. Goddard, *Phys. Rev. A* **12**, 1203 (1975).
- [81] K.D. Closser, O. Gessner, and M. Head-Gordon, *J. Chem. Phys.* **140**, 134306 (2014).
- [82] D.S. Peterka, *Imaging Chemical Dynamics with the Vacuum Ultraviolet* (University of California, Berkeley, 2005), Vol. 3211486.
- [83] J.P. Hernandez, *Rev. Mod. Phys.* **63**, 675 (1991).
- [84] M. Fámik and J.P. Toennies, *J. Chem. Phys.* **118**, 4176 (2002).
- [85] W. Schoepe and G. Rayfield, *Phys. Rev. A* **7**, 2111 (1973).
- [86] D.G. Onn and M. Silver, *Phys. Rev.* **183**, 295 (1969).
- [87] B. Schütte, M. Arbeiter, T. Fennel, M.J.J. Vrakking, and A. Rouzée, *Phys. Rev. Lett.* **112**, 073003 (2014).
- [88] J.H. Kim, D.S. Peterka, C.C. Wang, and D.M. Neumark, *J. Chem. Phys.* **124**, 214301 (2006).
- [89] D.S. Peterka, J.H. Kim, C.C. Wang, and D.M. Neumark, *J. Phys. Chem. B* **110**, 19945 (2006).
- [90] C.C. Wang, O. Kornilov, O. Gessner, J.H. Kim, D.S. Peterka, and D.M. Neumark, *J. Phys. Chem. A* **112**, 9356 (2008).
- [91] D.S. Peterka, J.H. Kim, C.C. Wang, and D.M. Neumark, *J. Phys. Chem. B* **110**, 19945 (2006).
- [92] K. von Haeften, T. Laarmann, H. Wabnitz, and T. Möller, *Phys. Rev. Lett.* **87**, 153403 (2001).
- [93] M.P. Ziemkiewicz, C. Bacellar, D.M. Neumark, and O. Gessner, *Test of Atomic Helium Signal Contributions in a Helium Nanodroplet Photoelectron Imaging Experiment* (unpublished).
- [94] P. O’Keeffe, Y. Ovcharenko, M. Ziemkiewicz, V. Lyamayev, M. Devetta, A. LaForge, O. Plekan, P. Finetti, M.D. Fraia, M. Krikunova, P. Piseri, M. Coreno, R. Richter, K.C. Prince, M. Drabbels, C. Callegari, O. Gessner, D. Neumark, F. Stienkemeier, T. Möller, and M. Mudrich, in preparation.
- [95] J. Reho, C. Callegari, J. Higgins, W.E. Ernst, K.K. Lehmann, and G. Scoles, *Faraday Discuss.* **108**, 161 (1997).
- [96] J. Reho, J. Higgins, K. Lehmann, and G. Scoles, *J. Chem. Phys.* **113**, 9694 (2000).
- [97] G. Droppelmann, O. Bünermann, C.P. Schulz, and F. Stienkemeier, *Phys. Rev. Lett.* **93**, 023402 (2004).
- [98] C.P. Schulz, P. Claas, and F. Stienkemeier, *Phys. Rev. Lett.* **87**, 153401 (2001).
- [99] B.E. Callicoatt, K. Förde, L.F. Jung, T. Ruchti, and K.C. Janda, *J. Chem. Phys.* **109**, 10195 (1998).
- [100] M. Schlesinger, M. Mudrich, F. Stienkemeier, and W.T. Strunz, *Chem. Phys. Lett.* **490**, 245 (2010).
- [101] H. Schmidt, J. von Vangerow, F. Stienkemeier, A.S. Bogomolov, A.V. Baklanov, D.M. Reich, W. Skomorowski, C.P. Koch, and M. Mudrich, *J. Chem. Phys.* **142**, 044303 (2015).